THE ASTROPHYSICAL JOURNAL, 506:758–772, 1998 October 20

CARBON RECOMBINATION LINES BETWEEN 34.5 AND 770 MHz TOWARD CASSIOPEIA A

NIMISHA G. KANTHARIA[1] AND K. R. ANANTHARAMAIAH[2]
Raman Research Institute, C.V. Raman Avenue, Bangalore 560 080, India

AND

H. E. PAYNE
Space Telescope Science Institute, 3700 San Martin Drive, Baltimore, MD 21218
Received 1997 December 8; accepted 1998 May 7

ABSTRACT

We present observations of low-frequency recombination lines of carbon toward Cas A near 34.5 MHz ($n \sim 575$) using the Gauribidanur radio telescope and near 560 MHz ($n \sim 225$) and 770 MHz ($n \sim 205$) using the NRAO 140 foot (43 m) telescope in Greenbank. We also present high angular resolution (1′) observations of the C270α line near 332 MHz using the Very Large Array in B-configuration. A high signal-to-noise ratio spectrum is obtained at 34.5 MHz, which clearly shows a Voigt profile with distinct Lorentzian wings, resulting from significant pressure and radiation broadening at such high quantum numbers. The emission lines detected near 332, 550, and 770 MHz, on the other hand, are narrow and essentially Doppler-broadened. The measured Lorentzian width at 34.5 MHz constrains the allowed combinations of radiation temperature, electron density, and electron temperature in the line-forming region. Radiation broadening at 34.5 MHz places a lower limit of 115 pc on the separation between Cas A and the line-forming clouds. Modeling the variation in the integrated line-to-continuum ratio with frequency indicates that the region is likely to be associated with the cold atomic hydrogen component of the interstellar medium, and the physical properties of this region are likely to be $T_e = 75$ K, $n_e = 0.02$ cm^{-3}, $T_{R100} = 3200$ K, and $n_{\rm H} T_e = 10{,}000$ cm^{-3} K. Comparison of the distribution of the C270α recombination line emission across Cas A with that of ^{12}CO and H I also supports the above conclusion.

Subject headings: H II regions — ISM: individual (Cassiopeia A) — line: profiles — radio lines: ISM

1. INTRODUCTION

The interstellar medium in the direction of the strong radio source Cas A ($l = 111\overset{\circ}{.}7$, $b = -2\overset{\circ}{.}1$) has been extensively studied in radio recombination lines of carbon. Konovalenko & Sodin (1980) were the first to observe a low-frequency (26.3 MHz) absorption line toward Cas A, which was later correctly identified as the 631α recombination line of carbon by Blake, Crutcher, & Watson (1980). Since then, this direction has been studied in many transitions in carbon with principal quantum numbers ranging from $n = 766$ to $n = 166$, which correspond to frequencies ranging from 14 to 1400 MHz, respectively (Konovalenko 1990; Payne, Anantharamaiah, & Erickson 1989, 1994, and references therein). Because Cas A is a strong radio source that dominates the system temperature at all these frequencies even for modest-sized antennas, the results of all these observations, which are conducted with varying beams, can be compared and used to constrain physical models of the line-forming gas.

In their observations of carbon recombination lines toward Cas A in the frequency range 34–325 MHz, Payne et al. (1989, hereafter PAE89) detected a smooth transition from absorption to emission with increasing frequency; the lines are in emission at frequencies above 200 MHz and in absorption below 115 MHz. At frequencies where lines are seen in emission, the line widths are essentially due to Doppler broadening, and the carbon line spectra show two main components at velocities near -37 km s^{-1} and -48 km s^{-1} that correspond to the Perseus arm in this direction. In some earlier observations, a weak component near -1 km s^{-1} corresponding to the Orion arm has also been reported (PAE89) in this direction. However, at lower frequencies (large n) where the lines appear in absorption, pressure and radiation broadening causes the two Perseus arm components to blend into a single feature. This spectral broadening results in Voigt profiles that have a narrow Gaussian-like shape in the central region (due to Doppler broadening) and broad Lorentzian wings. Observationally, it has been difficult to detect the Lorentzian wings in the low-frequency recombination lines because of practical problems such as weakness of the line and incorrect baseline removal from the observed spectrum. The procedures that are generally used for baseline removal may reduce the amplitude of the Lorentzian wings, thus leading to wrong values of line widths and line strengths. Sorochenko & Smirnov (1990) noted that the reported widths and strengths of the low-frequency lines were based on Gaussian profiles instead of Voigt profiles, and they applied corrections to the integrated optical depths ($\int \tau\, dv$) by assuming the latter. More recently, Payne et al. (1994, hereafter PAE94) have quantitatively shown that the baseline-removal procedure has led to an underestimation of both the line strength and the line width. They constructed model line profiles using probable cloud parameters and showed that at the lowest frequencies, the integrated optical depths of the observed lines could have been underestimated because of baseline removal by a factor of almost 3. At higher frequencies, the observed profiles matched well with their model profiles.

For most of the last 18 years since the low-frequency carbon recombination lines were first detected toward Cas A, two types of models have been under debate: (1) the warm gas model with electron temperature T_e in the range

[1] Joint Astronomy Programme, Indian Institute of Science, Bangalore 560 012, India.

[2] Also at the National Radio Astronomy Observatory, New Mexico 87801.

35–75 K and electron density n_e in the range 0.05–0.1 cm^{-3}, which could be coexistent with the H I phase of the interstellar medium (ISM; Blake et al. 1980; Konovalenko & Sodin 1981; Walmsley & Watson 1982; PAE89; PAE94) and (2) the cold gas model with $T_e \sim 16$–20 K and $n_e \sim 0.3$ cm^{-3} (Ershov et al. 1984, 1987), which could be coexistent with the molecular hydrogen component of the ISM. Ershov et al. (1984, 1987) showed that the cold gas model explained their observations better than the warm gas model and suggested that the carbon recombination lines could originate in small (≤ 1 pc), dense ($n_{\rm H} = 10^3$–10^4 cm^{-3}) clouds where the main agent for ionizing carbon would be diffuse ultraviolet radiation.

However, PAE94 have provided evidence that shows strong support for the warm gas model. Based on data spanning almost two decades in frequency, PAE94 have developed a model that satisfactorily explains the observed variation of integrated optical depth with principal quantum number. The parameters of their model provide thermal balance in the clouds and pressure equilibrium with the environment. Their model is also consistent with the 21 cm H I absorption observations toward Cas A. In this model, PAE94 have considered a new boundary condition ($b_n \rightarrow 0$ as $n \rightarrow n_{\rm critical}$) suggested by Gulyaev & Nefedov (1989) for calculating the departure coefficients b_n and also included the occupation probabilities of high quantum number levels, which are affected by the presence of electrons and neutral particles in the cloud (Hummer & Mihalas 1988). The one parameter that the model by PAE94 is unable to explain is the width of the lines, which is better explained by earlier models that used the boundary condition $b_n \rightarrow 1$ as $n \rightarrow \infty$ and had dielectronic-like recombination effects (Watson, Western, & Christensen 1980; Walmsley & Watson 1982; Sorochenko & Walmsley 1991) included in the calculation of b_n.

In this paper, we present high-sensitivity carbon recombination line observation near 34.5 MHz made using the Gauribidanur radio telescope. A high signal-to-noise ratio spectrum is obtained, which, after the removal of a simple linear baseline, clearly shows a Voigt profile with distinct Lorentzian wings, as expected. This leads to a reliable estimate of the integrated optical depth at a low frequency where the line width is dominated by pressure or radiation broadening. We also present carbon recombination line observations at 560 and 770 MHz made using the NRAO 140 foot (43 m) telescope at Green Bank, where the line width is essentially due to Doppler broadening. Furthermore, the spatial distribution of the carbon recombination lines near 332 MHz over the face of Cas A ($\alpha_{1950} = 23^{\rm h}21^{\rm m}10^{\rm s}$, $\delta_{1950} = 58°32'29''$) is obtained with an angular resolution of 25″ (later convolved to 1′) using the B-configuration of NRAO's VLA, and the distribution is compared with that of ^{12}CO emission and 21 cm H I absorption with similar angular resolution. Finally, we present a reexamination of the existing models in the light of these new observations.

2. OBSERVATIONS AND RESULTS

2.1. *Gauribidanur Observations near 34.5 MHz*

The low-frequency dipole array at Gauribidanur which operates near 34.5 MHz (Deshpande, Shevgaonkar, & Shastry 1989 and references therein) was used during 1995 July–October to observe several α transitions ($\Delta n = 1$) with principal quantum numbers ranging from $n = 570$ to 580. The Gauribidanur radio telescope is a meridian transit instrument consisting of 1000 broad-band dipoles arranged in a T shape. The east-west (EW) arm consists of 640 dipoles, distributed over a distance of 1.38 km, whereas the north-south arm extends southward from the center of the EW arm and consists of 360 dipoles laid over a distance of 0.45 km. The present set of observations were carried out using the EW arm in total power mode, which gave an angular resolution of 21′ × 25° ($\alpha \times \delta$) at zenith. The effective collecting area of the EW arm is $160\lambda^2$ ($\lambda = 8.67$ m).

The Gauribidanur telescope has limited tracking facility (Deshpande et al. 1989) that enables the array to track a source for a period of 40 sec δ minutes about its transit time. Since Cas A ($\delta \sim 58\overset{\circ}{.}8$) could be observed only for ~ 80 minutes a day, it would have taken almost a week to detect the expected absorption line with a signal-to-noise ratio of ~ 5. To reduce the total duration of observations, we employed a multiline receiver in which eight different transitions with $\Delta n = 1$ near $n = 575$ were observed simultaneously. Since information carried by the recombination lines changes slowly with the quantum number, these adjacent spectra can be averaged to effectively increase the integration time. At 34.5 MHz, the successive recombination lines are separated in frequency by ~ 180 kHz, and therefore 11 of these transitions fall within the 2 MHz observing band. We selected eight transitions (C571α–C578α) that were relatively free of interference and made observations with the eight-line spectrometer specially developed for this purpose. In practice, we found that, on an average, two out of the total eight bands were corrupted by interference.

To realize the eight-line receiver, the combined 34.5 MHz signal from the EW arm with a bandwidth of 2 MHz was first translated to a 4 MHz intermediate frequency using a first local oscillator near 30.5 MHz. This band was further translated to 8 base bands, each with a bandwidth of 32 kHz, using 8 second local oscillators in such a way that the center of these 32 kHz bands corresponded to the eight recombination line frequencies. The second conversion actually "folded" the upper and lower sidebands (spanning a bandwidth of 64 kHz) into a single base band of 32 kHz. The two sidebands near each of the eight transitions were later "unfolded" using digital techniques to obtain two independent 32 kHz spectra with a resolution of 0.3 kHz. One of these spectra (the upper sideband or the lower sideband) contained the expected recombination line, and the other was regarded as a reference spectrum that could be used to correct for the instrumental response. The spectral line was switched at a rate of 2 s between the upper sideband and lower sideband by switching the first local oscillator by 32 kHz. This method resulted in remarkably good baselines; only a linear baseline had to be removed from the final integrated spectrum, which has an effective integration time of ~ 400 hr. A 128 channel, double sideband, one-bit digital correlator running at 1 MHz (Ravindra 1983; Udayashankar 1986) was used to sequentially process the eight 32 kHz "folded" base bands, which were effectively sampled at a rate of 128 kHz. Memory banks were used to temporarily store the sampled data for sequential processing.

The data collected were carefully examined and all those affected by interference were removed. The final spectrum, which is an average of all the observed transitions, is shown in Figure 1. The spectrum is Hanning smoothed and therefore has a resolution of 0.5 kHz (4.4 km s^{-1}).

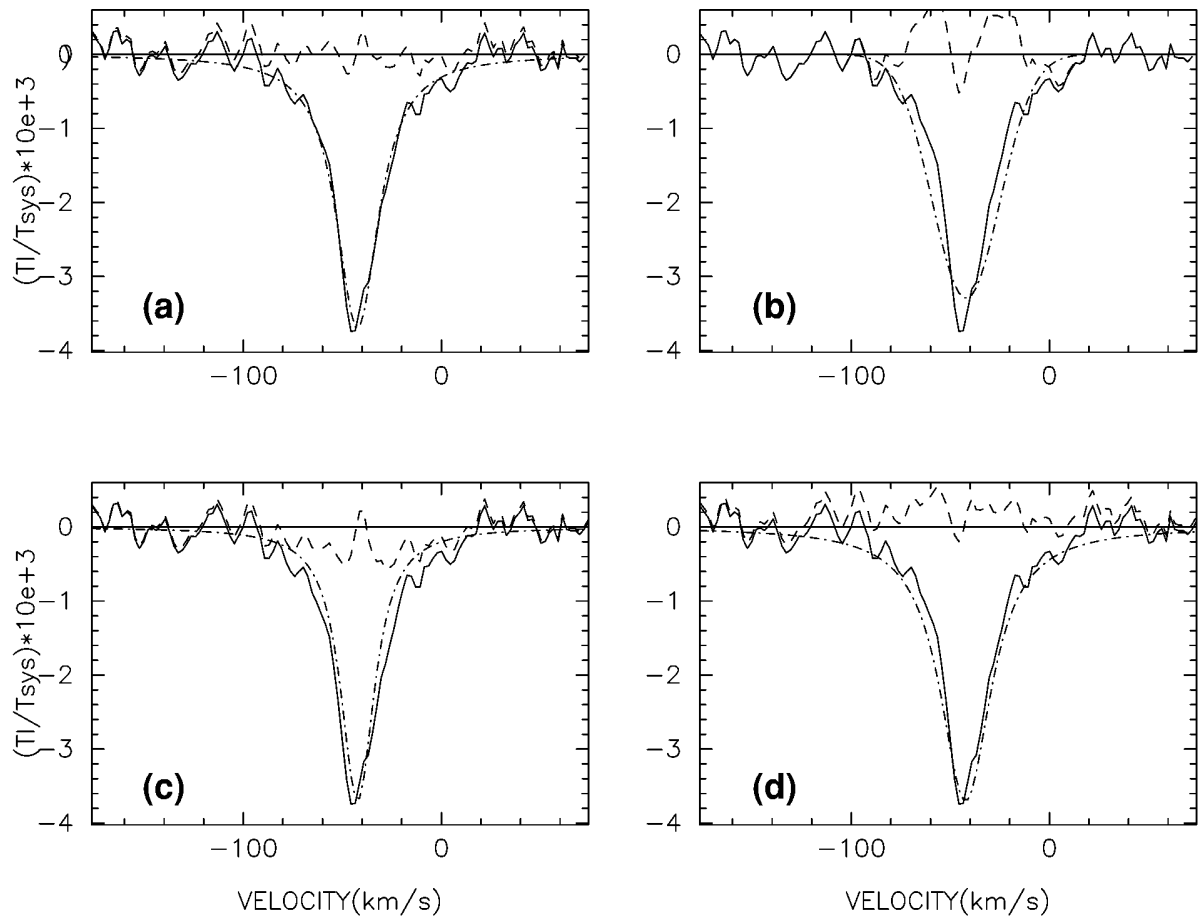

FIG. 1.—Spectrum observed toward Cas A at 34.5 MHz. The solid line shows the observed spectrum, the dash-dotted line shows the model fit, and the dashed line shows the residuals. In (*a*), the best-fitting Voigt profile is superposed on the observed spectrum; in (*b*), the best-fitting Gaussian profile is shown. In (*c*) and (*d*), Voigts enclosing 20% less and 20% more area are shown. The fit parameters of the best-fitting Voigt are $T_l/T_{sys} = -3.7(0.1) \times 10^{-3}$, radial velocity is $-42(0.3)$ km s^{-1}, Doppler width is 3.5 km s^{-1}, and Lorentzian width is 25.40(0.69) km s^{-1}.

The spectrum in Figure 1 clearly shows the presence of wings, which is expected at these frequencies because of the dominance of radiation and pressure broadening. These wings had not been observed so clearly in earlier observations owing to either poor signal-to-noise ratio or to improper bandshape corrections. It is clear that a Gaussian profile is a poor realization of this spectrum, as illustrated in Figure 1*b*, where the best-fitting Gaussian has been superposed over the observed spectrum, and the residuals after subtracting the Gaussian are shown as a dashed line. On the other hand, a Voigt profile provides a much better fit as shown in Figure 1*a*. The fitted parameters of the Voigt are listed in Table 1. The Doppler width was fixed at 3.5 km s^{-1} as obtained from our spectrum at 770 MHz (see below). To show that the best-fitting Voigt profile in Figure 1*a* has not overly underestimated the integrated optical depth because of the possible extension of the weak Lorentzian wings beyond the observed spectrum, we show in Figures 1*c* and 1*d* Voigt profiles that enclose 20% less and 20% more area, respectively, by adjusting the Lorentzian width. It is clear that in both cases the central core of the spectrum is not fitted well. The same result is obtained if the peak optical depth is varied while holding the Lorentzian width fixed or by varying both the parameters simultaneously. Thus, the relatively high signal-to-noise ratio of the central absorption in Figure 1 rules out these alternate fits. We, therefore, believe that any uncertainty in the determination of the zero level of the spectrum in Figure 1 causes $<20\%$ error in the estimated integrated optical depth noted in Table 1.

A closer inspection of the observed spectrum in Figure 1 reveals a slight asymmetry in the profile near 0 km s^{-1}, which could probably be due to the Orion arm component.

TABLE 1

LINE FIT PARAMETERS

Number	ν (MHz)	Cnα	T_l/T_c (10^{-3})	V_{lsr} (km s^{-1})	ΔV_D (km s^{-1})	ΔV_L (km s^{-1})	$\int \tau\, dv$ (s^{-1})
1	34.5	571–578	-3.7 ± 0.8	-42.3 ± 0.2	3.5	25 ± 5	16.1 ± 3.2
2	332	270	2.5 ± 0.5	-47.3 ± 0.6	5.7 ± 0.8	...	-19.7 ± 3.8
3	560	223, 224	0.78 ± 0.06	-46.4 ± 0.2	3.6 ± 0.2	...	-11.8 ± 0.8
		225, 226, 229	0.24 ± 0.04	-36.7 ± 0.7	8.4 ± 1.1	...	...
4	770	201, 202, 205	0.57 ± 0.02	-48.4 ± 0.1	3.5 ± 0.1	...	-8.2 ± 0.5
		206	0.11 ± 0.02	-39.5 ± 0.4	4.1 ± 0.6	...	...

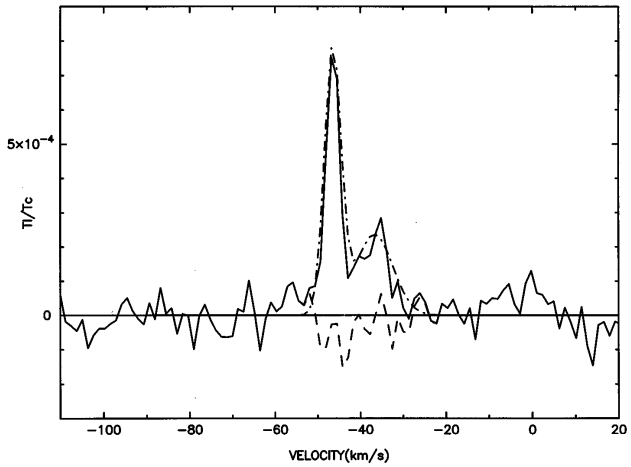

FIG. 2.—C225α spectrum toward Cas A at 560 MHz

However, an even higher signal-to-noise spectrum is required to confirm this.

2.2. *NRAO 140 Foot Telescope Observations at 560 MHz and 770 MHz*

Observations near 770 MHz ($n \sim 205$, $\lambda \sim 39$ cm) and 560 MHz ($n \sim 226$, $\lambda \sim 53$ cm) were obtained on the NRAO 140 foot telescope at Greenbank during 1991 September. We used the spectral processor to observe four transitions simultaneously in two orthogonal circular polarizations, increasing the integration time by a factor of 8. On average, however, at least one of the eight receivers was corrupted by interference. To further increase the effective integration time, data were obtained by frequency switching so that the carbon line frequencies were always within the observing band. Final spectra were obtained by folding to average both halves of the observing band. The effective integration times are 279 and 81 hr at 770 and 560 MHz, respectively. The velocity resolution at 560 MHz is 1.3 km s^{-1}, and at 770 MHz it is 1 km s^{-1}. The observed spectra in units of the line to continuum ratio are shown in Figures 2 and 3. Both the Perseus arm features are clearly observed in the spectra at the two frequencies. The −48 km s^{-1} feature is 3–4 times stronger than the feature at −37 km s^{-1}. The line fit parameters are listed in Table 1. The line widths have been corrected for the instrumental resolution. Only statistical errors are included.

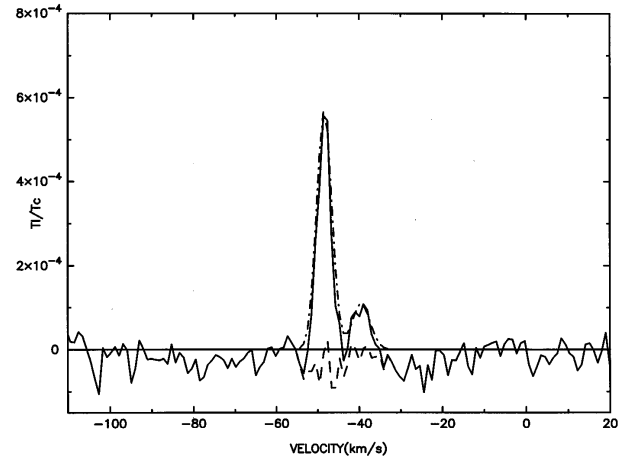

FIG. 3.—C205α spectrum toward Cas A at 770 MHz

2.3. *VLA Observations at 332 MHz*

Cas A was observed in four sessions during 1991 December in the B-configuration of the VLA for a total telescope time of 10 hr. The C270α ($\nu = 332.419$ MHz) line emission across Cas A was imaged with an angular resolution of 27″ × 21″. The program source was observed for 35 minutes at a stretch, while observations of 2348+643 were interspersed to calibrate the phase. The primary and bandpass calibrators were observed once during each session. More details of these observations are listed in Table 2.

The UV data were processed using the Astronomical Image Processing System (AIPS) developed by NRAO. The "Ch 0" image was generated by averaging the visibilities in the central three-quarters of the band. These visibility data were edited and calibrated using the phase and amplitude calibrators. The procedure MX in AIPS, which uses the CLEAN algorithm, was used to generate the continuum brightness distribution free of sidelobe responses. Natural weighting of the data gave a beam size of 27″ × 21″.

Because bandpass calibration involves dividing the source spectrum with the bandpass of the calibrator for each antenna, it is essential to choose a calibrator whose signal-to-noise ratio is comparable to or more than that of the program source. Cas A with a flux density of ∼6000 Jy near 330 MHz is one of the strongest radio continuum sources in the sky, and so Cyg A, which has a comparable flux density at this frequency, was chosen as the bandpass calibrator. Since Cyg A has spatial structure that begins to get resolved on the longer baselines, the signal-to-noise ratio of the antenna bandpasses were not uniform. However, experimenting with an unresolved weaker source as the bandpass calibrator, we found that the results obtained with Cyg A were better than those with the weaker source, and hence we used Cyg A as the bandpass calibrator. The line data were calibrated for amplitude, phase, and bandpass using standard procedures. The continuum

TABLE 2

DETAILS OF VLA OBSERVATIONS

Number	Parameter	
1.....	Field center: α(1950)	$23^h21^m10^s$
	δ(1950)	58°32′29″
2.....	Observing sessions	1991 December
3.....	Telescope time	10 hr
4.....	Observed transitions	C270α
5.....	Rest frequencies (carbon)	332.419 MHz
6.....	Observing band	P-band (90 cm)
7.....	Primary beam	150′
8.....	VLA antenna configuration	B
9.....	Shortest spacing	0.21 km
10	Longest spacing	11.4 km
11	Observing mode	2AC
12	Expected T_{sys}	>750 K
13	Total bandwidth	98 kHz (88 km s^{-1})
14	Number of channels	128
15	Frequency resolution	1.526 kHz
16	Velocity resolution	1.38 km s^{-1}
17	Amplitude calibrator	3C48
18	Phase calibrator	2348+643
19	Bandpass calibrator	Cyg A
20	Synthesized beam (natural weighting)	27″ × 21″
21	rms noise, line	35 mJy $beam^{-1}$
22	rms noise, continuum	375 mJy $beam^{-1}$

emission was subtracted from the visibilities using the task UVLIN, and HORUS was used to image the residual line visibilities after applying natural weighting. The images where line emission was detected were deconvolved using the CLEAN algorithm.

The continuum image of Cas A at 330 MHz with a beam of $27'' \times 21''$ (P.A. $= -79°$) is shown in Figure 4. The shell-like morphology of Cas A is clearly seen. The continuum structure also consists of knots of emission, and the brightest region occurs in the west of the source. The integrated continuum flux density of Cas A is 6050 Jy, which is about 5.4% higher than that estimated by Baars et al. (1977). This excess flux is an artifact of the errors in the correction of the digitally measured visibility function (Bieging, Goss, & Wilcots 1991), which occurs in the VLA correlator system for strong sources like Cas A. This error is likely to be smaller in the optical depth maps, which are formed from the ratio of the line to continuum strengths. The observed peak continuum and peak line brightness are 145 Jy beam^{-1} and 0.7 Jy beam^{-1}, respectively. The rms noise on the continuum image is 375 mJy beam^{-1}, and on the line image the rms noise is 35 mJy beam^{-1}.

The spectrum in units of line to continuum ratio (S_l/S_c) is shown in Figure 5. To obtain this spectrum, the line emission was integrated over the continuum source and divided by the integrated continuum emission. A Perseus arm component of amplitude 2.5×10^{-3} and width ~ 5 km s^{-1} is clearly detected at -47 km s^{-1}. We do detect some emission from the second Perseus arm component near -38 km s^{-1}. However, the rms noise in the spectrum is $\sim 7 \times 10^{-4}$, and since the spectral features near -38 km s^{-1} and 0 km s^{-1} are of the order of 1×10^{-3} (Anantharamaiah et al. 1994), these features require a higher signal-to-noise spectrum to be significant.

The observed C270α emission across Cas A, where the continuum intensity exceeds 10 Jy beam^{-1}, is shown for different radial velocities (-39.8 to -49.4 km s^{-1}) in Figure 6. The different images are separated in velocity by 1.4 km s^{-1}. Line emission is strongest near -46.6 km s^{-1}. The emission is patchy. The morphology traced by the line emission resembles the continuum morphology, particularly in the southern and western regions. This is direct evidence of stimulated emission, since the continuum radiation is from the nonthermal emission of the supernova

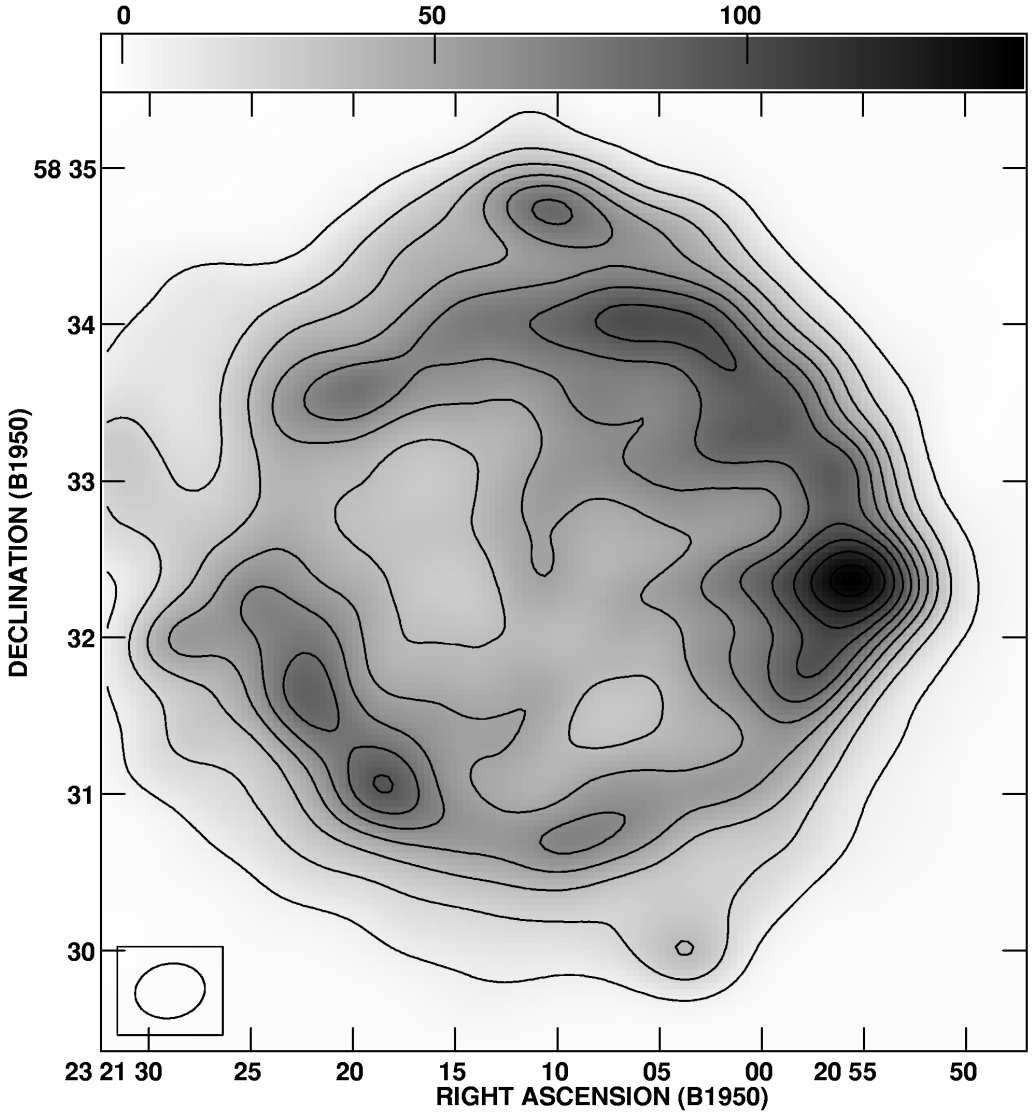

FIG. 4.—Continuum image of Cas A at 330 MHz. Angular resolution is $27'' \times 21''$, and P.A. $= -79°$. The contour levels are 1, 3, 5, 7, 9, 11, 13, 15, 17, 19, and 20 in units of 7.2 Jy beam^{-1}. The gray-scale flux range is -2.4 to 144 Jy beam^{-1}.

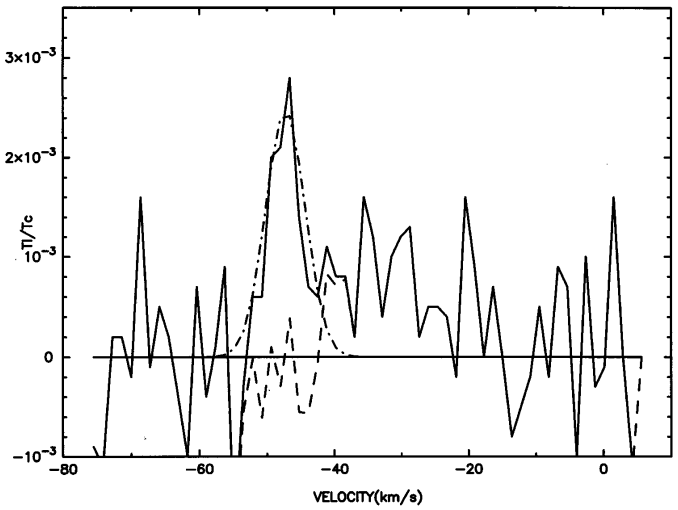

FIG. 5.—Global C270α spectrum of Cas A obtained using the VLA. The dash-dotted curve represents a Gaussian fit, and the residuals are shown as dashed lines.

remnant whereas the recombination line emission arises in the foreground thermal gas. The positions of peak emission appear to be slightly different for different velocities. At -46.6 km s^{-1}, the western and southern parts of Cas A have the strongest intensity. The line brightness is weaker at -49.4 km s^{-1}, but it appears to be spread out in patches over almost the entire continuum disk. We also detect weak emission at velocities of -39.8 and -41.1 km s^{-1}, which correspond to the second Perseus arm component. However, the signal-to-noise ratio is low at these velocities. These are the highest resolution recombination line images of Cas A at this frequency.

In Figure 8, the optical depth images obtained from the line and continuum images of Cas A are shown. The optical depth at each point in the image is calculated from the quantity $\ln (S_l/S_c + 1)$ using the task COMB in AIPS. The largest optical depths are seen near the edge and from the central regions of the continuum source. The highest optical depth occurs at -46.6 km s^{-1}. The presence of the secondary peaks near the center of Cas A indicates inhomogeneities in the foreground thermal gas. Comparison of these images with the distribution of the H I 21 cm line and the molecular lines at comparable spatial and spectral resolutions across Cas A is presented in § 3.2.

3. PROPERTIES OF THE LINE-FORMING REGION

3.1. *Physical Limits from Observed Line Width*

The carbon recombination line toward Cas A appears in absorption at 34.5 MHz and in emission near 332, 560, and 770 MHz, as shown in Figures 1, 2, 3, and 5. There is a dramatic difference in the line width at 34.5 MHz and the other frequencies. It is clear that pressure and/or radiation broadening, both of which are strong functions of frequency, is responsible for the large line width at 34.5 MHz. The higher frequency lines are broadened essentially by thermal or turbulent motions in the cloud. While the measured width of the lower frequency line can be used to constrain the radiation field surrounding the clouds and the electron density in the clouds, the higher frequency observations would be useful to obtain limits on the temperature

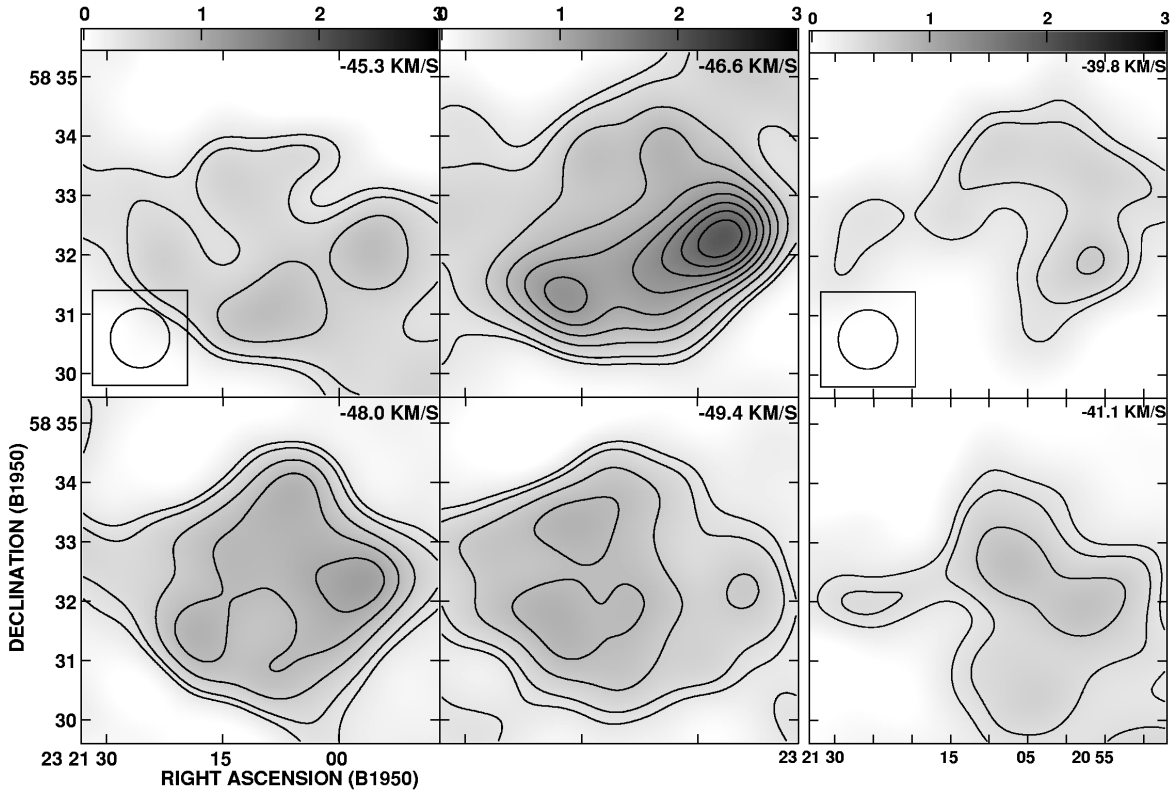

FIG. 6.—Distribution of C270α line emission across Cas A at different radial velocities corresponding to the Perseus arm. The full resolution (∼30″) maps have been smoothed to an angular resolution of ∼1′. The beam is depicted in the inset and the radial velocity is noted in the upper right corner of each frame. The contour levels represent 1.5, 2, 3, 4, 5, 6, 7, 8, 9, and 10 in units of 0.2 Jy beam^{-1}. The gray-scale flux range is 0–3 Jy beam^{-1}.

and to constrain possible association with H I or molecular clouds. We obtain a not-too-significant upper limit of 3800 K for the electron temperature of the cloud from the width of the -47 km s^{-1} Perseus arm feature at 560 MHz. The -39 km s^{-1} Perseus arm feature has a width of 5.4 km s^{-1} at 770 MHz, which implies an upper limit of $\sim$7600 K for this gas. The variation in the Doppler width of the -47 and -39 km s^{-1} features observed at different frequencies (see Table 1) is likely to be a result of velocity resolution and other instrumental effects.

The line width due to radiation broadening can be calculated using

$$\Delta V_R = 8 \times 10^{-20} W_v T_{R100} n^{5.8} \frac{c/(\text{km s}^{-1})}{\nu/(\text{kHz})} \text{ km s}^{-1} \quad (1)$$

(Shaver 1975), where T_{R100} is the radiation temperature of the background radiation field at 100 MHz ($\alpha = 2.6$) and $W_v = [\Omega(s)/4\pi]$ m, where $\Omega(s)$ is the solid angle of the source of radiation seen by the cloud. At low temperatures, the line width due to pressure broadening can be calculated using

$$\Delta V_P = 2 \times 10^{-8} \exp\left(-\frac{26}{T_e^{1/3}}\right) \frac{N_e n^{5.2}}{T_e^{1.5}} \frac{c/(\text{km s}^{-1})}{\nu/(\text{kHz})} \text{ km s}^{-1} \quad (2)$$

(Shaver 1975).

If the entire Lorentzian width of 25.4 km s^{-1} at 34.5 MHz is assumed to be due to radiation broadening, then equation (1) gives an upper limit of 3600 K for $W_v T_{R100}$. The value $W_v T_{R100}$ is sum of two parts: the contribution from the galactic nonthermal background $W_{v,bg} T_{R100,bg}$ and the contribution from Cas A, $W_{v,\text{Cas A}} T_{R100,\text{Cas A}}$. Since the Galactic background around Cas A, $T_{R100,bg} \sim 800$ K (Haslam et al. 1982) and $W_{v,bg} = 1$, the upper limit to $T_{R100,\text{Cas A}}$ is $\sim$2400 K. Taking the distance to Cas A to be 3.4 kpc and its linear size to be 5 pc and using the flux density from Baars et al. (1977) of $S_{100} = 12,300$ Jy, the brightness temperature of Cas A at 100 MHz is 1.85×10^7 K. The upper limit derived above thus translates to a lower limit to the distance between Cas A and the line-forming cloud of 115 pc.

Pressure broadening depends directly on the electron density, and it is also a weak function of electron temperature ($\propto T_e^{-0.1}$). If the cloud is far away from Cas A and therefore subjected to only the Galactic nonthermal radiation field (i.e., $T_{R100} = 800$ K), then for an electron temperature of 75 K, which is typical of H I clouds, the observed Lorentzian width of 25.4 km s^{-1} implies an electron density of 0.15 cm^{-3}. If the temperature is as low as 20 K, which is typical of molecular clouds, then the implied electron density is 0.65 cm^{-3}. On the other hand, if the radiation temperature is four times the galactic background (i.e., $T_{R100} = 3200$ K), then the electron density is 0.02 cm^{-3} for $T_e = 75$ K and 0.08 cm^{-3} for $T_e = 20$ K. It is clear that, from the observed Lorentzian width, it is possible to obtain constraints only on the combination of electron density, temperature, and the radiation background. In Table 3, for $T_e = 75$ and 20 K, values of electron densities are given for three different values of radiation temperature T_{R100}. In Figure 7, the variation of the observed line width with quantum number is shown. The points indicate the observed data, whereas the curves show the model fits from Table 3 constrained by our observation at 34.5 MHz. All the models use a Doppler width of 3.5 km s^{-1}, which fits the higher frequency data well. The bold circles are the present observations, the filled star is from Sorochenko & Walmsley (1991), and the filled circles and triangles are observations from Konovalenko (1984) and Lekht, Smirnov, & Sorochenko (1989), corrected for the expected Lorentzian wings by PAE94. All the other points are taken from Sorochenko & Smirnov (1990): the open squares are data from PAE89, the hexagram is data from PAE94, and the open stars are from Ershov et al. (1987). All the models given in Table 3 predict almost identical variations of line width with quantum number. It appears from Figure 7 that all the observations beyond $n = 600$ have still underestimated the line width.

TABLE 3

PARAMETERS CONSTRAINED FROM LINE WIDTH

T_e (K) (1)	T_{R100} (K) (2)	n_e (cm^{-3}) (3)	$n_H T_e$ (cm^{-3} K) (4)
	800	0.15	3.75×10^4
75.....	1600	0.11	2.75×10^4
	3200	0.02	0.5×10^4
	800	0.65	4.33×10^4
20.....	1600	0.46	3.1×10^4
	3200	0.08	0.53×10^4

NOTE.—These models assume $\delta_C \sim 1.0$.

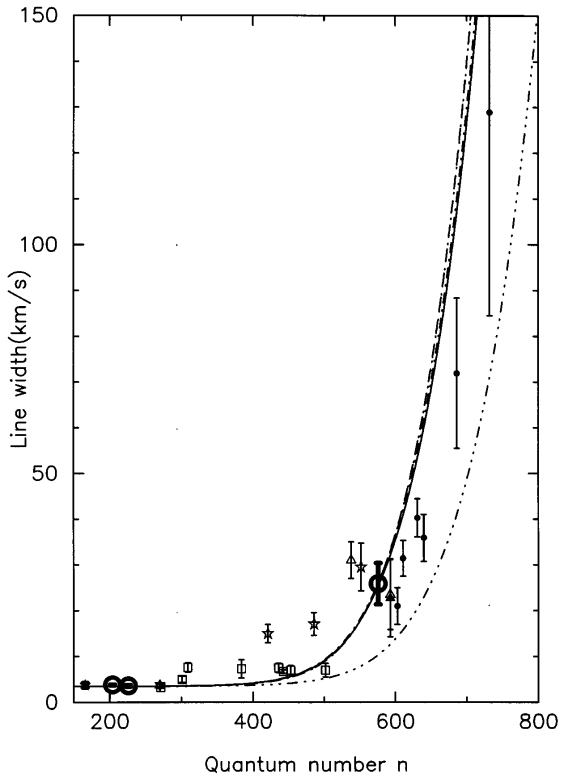

FIG. 7.—Data points show the observed variation in line width with quantum number. Our observations at 34.5, 560, and 770 MHz are shown by bold circles. The curves show the expected variation for different combinations of T_{R100}, T_e, and n_e for a Doppler width of 3.5 km s^{-1}. The curves for $T_e = 75$ K and combinations of $T_{R100} = 800$ K, $n_e = 0.15$ cm^{-3} and $T_{R100} = 3200$ K, $n_e = 0.02$ cm^{-3}; and for $T_e = 20$ K and combinations of $T_{R100} = 800$ K, $n_e = 0.65$ cm^{-3} and $T_{R100} = 3200$ K, $n_e = 0.08$ cm^{-3} are shown. The triple–dot-dashed curve is for $T_{R100} = 800$ K, $T_e = 35$ K, and $n_e = 0.05$ cm^{-3}.

If all the electrons in the cloud come from ionization of carbon (i.e., $n_e = n_C$) and if we assume a value for the abundance of carbon $[(n_C/n_H)]$ and its depletion factor (δ_C), then we can obtain an estimate of the thermal pressure in the cloud using $n_H T = [n_e/\delta_C(n_C/n_H)]T_e$.

Column (4) of Table 3 gives the values of $n_H T$ obtained using $\delta_C = 1$ (i.e., no depletion of carbon) and $(n_C/n_H) = 3 \times 10^{-4}$ (i.e., interstellar abundance). If the depletion is increased by some factor then the thermal pressure also increases by the same factor. The implied thermal pressure is high in all the models. Only models with high radiation temperature and no depletion give estimates that are closer to the interstellar thermal pressure. Most of the Galactic H I is believed to have a thermal pressure in the range 3000–5000 K cm^{-3} (McKee & Ostriker 1977; Kulkarni & Heiles 1988). However, Boulares & Cox (1990) show that the mean hydrostatic pressure in the galactic plane is $\sim$25,000 cm^{-3} K and is provided in almost equal measures by the magnetic field, cosmic rays, and thermal motions. This high overall pressure suggests that although coexistence with H I would favor similar thermal pressure for the carbon gas, it may not be a stringent requirement.

3.2. *Spatial Distributions of* C270α, ^{12}CO, *and* H I *Lines*

It is clear from the discussion above that, based on the width of the low-frequency recombination lines, the ionized carbon regions could be associated with either the cold ($T_e \sim 20$ K) molecular clouds in the direction of Cas A or the warmer ($T_e \sim 100$ K) atomic H I clouds. In order to get a further constraint on the possible association, we compare the spatial distribution of ionized carbon regions obtained over the face of Cas A from VLA observations of the C270α line with that of ^{12}CO and 21 cm H I line.

In Figure 8, we show the distribution of optical depth of the C270α line over the face of Cas A with a resolution of 1′ at four different radial velocities. These velocities correspond to the strong Perseus arm component near -47 km s^{-1}. The width of each channel is $\sim$1.4 km s^{-1}. The largest optical depths are in the channel with a radial velocity of -46.6 km s^{-1}. There is a gradient in the optical depth from east to west with the strongest optical depths at the western boundary. A secondary peak appears near the center in this velocity channel. In the channel with a center velocity of -45.3 km s^{-1}, there is a sharp gradient in the optical depth

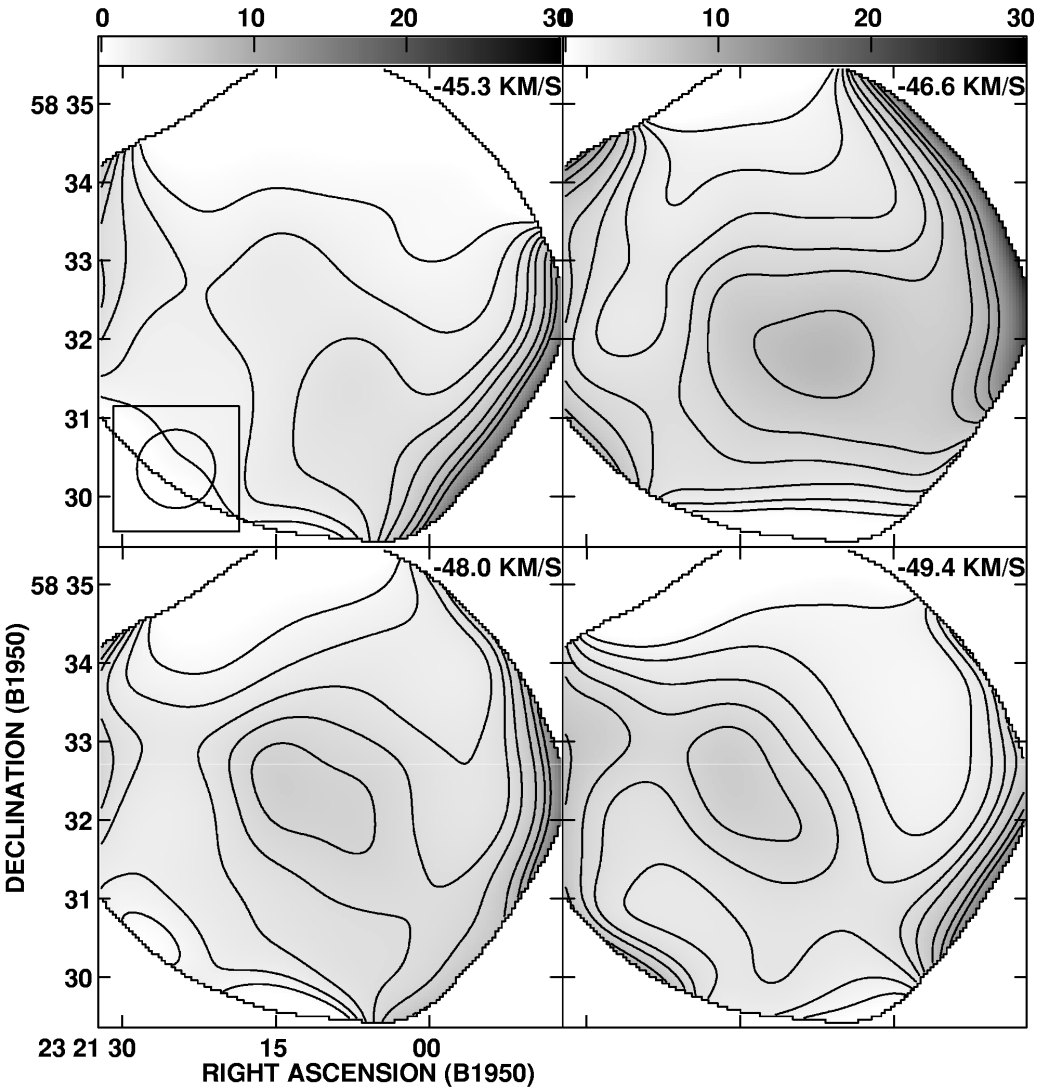

FIG. 8.—Variation in C270α optical depth observed across Cas A at different radial velocities. The gray-scale flux varies from 0 to 0.03. The contour levels are 1, 2, 3, 4, 5, 7, 9, and 11 in units of 0.001. The radial velocity is noted in the top right corner of each panel.

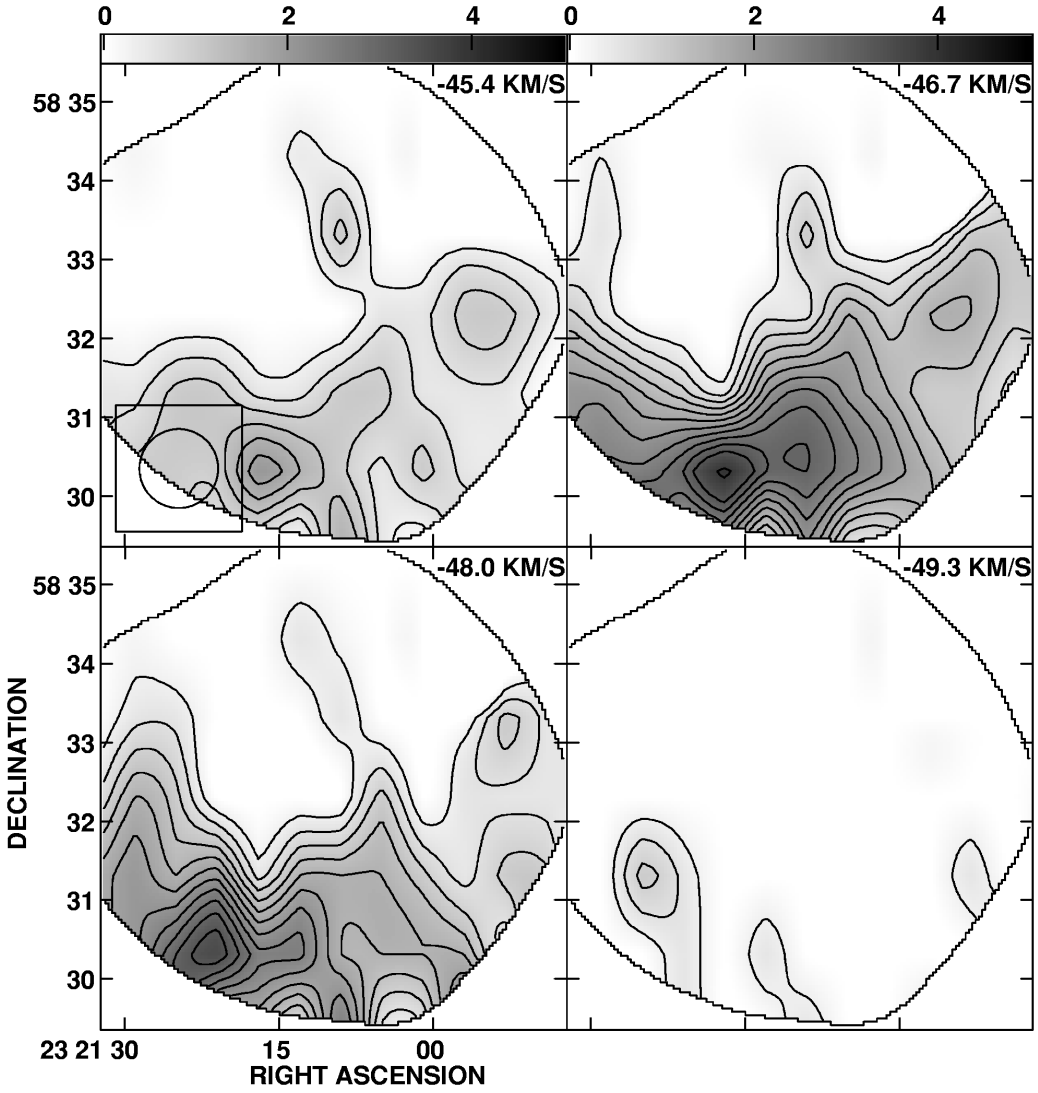

FIG. 9.—Variation in observed ^{12}CO emission across Cas A at different radial velocities. The gray-scale flux ranges from 0 to 5 K. The contour levels are 1, 2, 3, 4, 5, 6, 7, 8, 9, 10, 11, 13, and 15 in units of 0.3 K. The data are taken from Anantharamaiah et al. (1994).

from northeast to southwest. At the other two velocities (-48.0 and -49.4 km s^{-1}), the peak optical depth is near the center of Cas A.

For comparison, the ^{12}CO emission over the face of Cas A with the same resolution (i.e., 1′) is shown in Figure 9. These images were obtained from the ^{12}CO observation by Anantharamaiah et al. (1994) using the 10.4 m millimeter-wave telescope in Bangalore. It is clear from Figures 8 and 9 that the distribution of ^{12}CO and C270α lines are very different. For example, hardly any molecular emission is seen at a velocity of -49.3 km s^{-1}, whereas the same channel in C270α line shows considerable emission. At -46.7 and -48 km s^{-1}, the ^{12}CO emission has a strong concentration in the southeast region, which is not seen in the recombination line. We therefore conclude that the spatial structure of carbon recombination lines toward Cas A has very little similarity with the structure of molecular gas in that direction.

On the other hand, there is reasonable correspondence between the spatial distribution of the optical depths of the C270α recombination line and the 21 cm H I absorption line toward Cas A. In Figure 10, the distribution of H I optical depth across Cas A at different velocities is shown at a resolution of 1′. These maps have been obtained by convolving the high-resolution images (∼30″) of Schwarz, Goss, & Kalberla (1997) to a coarser resolution. Comparison with Figure 8 reveals better correspondence between the distributions of C270α and atomic H I gas, although the peaks of emission/absorption are not exactly coincident. The general trend displayed by the two is similar for all the four velocities shown in Figure 8. Although the positions of the peak H I optical depth do not exactly coincide with the peak C270α emission, enhanced H I absorption is observed at the peaks of C270α emission. The shift in positions could possibly be due to the smoothing of the high-resolution H I maps, which are saturated at certain velocities. Figure 11, taken from Anantharamaiah et al. (1994), shows the spatial distribution of the optical depths of C270α and H I line and ^{12}CO emission over four velocity ranges at which H I optical depths are not saturated. The images in Figure 11 are at a lower angular resolution of ∼2.′5. Correspondence between C270α and H I is particularly evident in two velocity ranges, viz., -45.3 to -46.6 km s^{-1} and -49.4 to -50.8 km s^{-1}. These two velocity ranges are on the wings

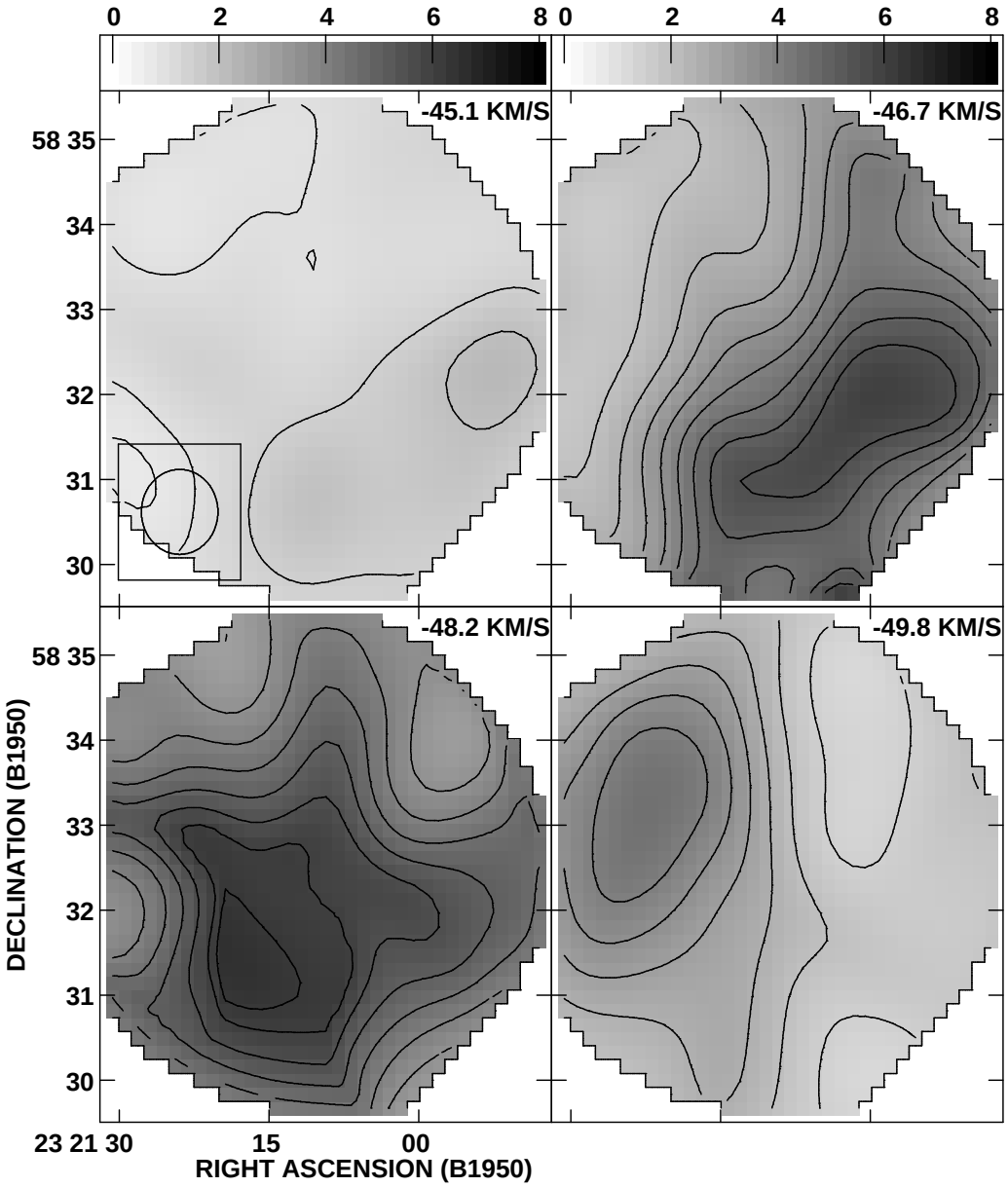

FIG. 10.—Variation in observed H I optical depth across Cas A at different radial velocities. The gray-scale flux ranges from 0 to 8. The contour levels are 1.5, 2, 3, 4, 5, 6, 7, 8, 9, 10, 11, and 12.5 in units of 0.5 K. The data are taken from Schwartz et al. (1997).

of the deep H I absorption feature found toward Cas A and therefore are not saturated. In these two velocity ranges, the position of the peaks and the direction of the gradient in the optical depths are very similar in C270α and H I maps. On the other hand, in these same velocity ranges the ^{12}CO distribution is completely different, and in fact there is hardly any ^{12}CO emission in the lower velocity range. There is, however, some similarity between all three distributions, i.e., C270α, H I, and ^{12}CO, in the velocity range -35.6 to -39.8 km s^{-1}.

On the whole, it does appear that the spatial distribution of C270α over the face of Cas A has better correspondence with that of H I distribution than with the distribution of ^{12}CO. This comparison thus favors the association of the carbon line region with the neutral H I component.

3.3. *Constraints from the Integrated Line Strength*

Carbon recombination lines toward Cas A have been observed over almost two decades in frequency -14 to 1400 MHz (Konovalenko 1990; PAE89; Sorochenko & Walmsley 1991). The direction of Cas A has the special advantage that, although the above observations have been made with widely varying beamwidths, a direct comparison of all the measurements can be made. This comparison is possible, because the continuum emission from Cas A, against which the lines are detected, overwhelms the total system temperature at all these frequencies, even for moderate-size telescopes. Therefore, the effective angular resolution of all these observations corresponds to the angular size of Cas A ($\sim 5'$) rather than to the beamwidths of the telescopes used.

A number of attempts have been made to construct models that could satisfactorily explain the observations (e.g., Walmsley & Watson 1982; Ershov et al. 1984, 1987; PAE89; Sorochenko & Walmsley 1991; PAE94). In this section, we reexamine some of these models in the light of

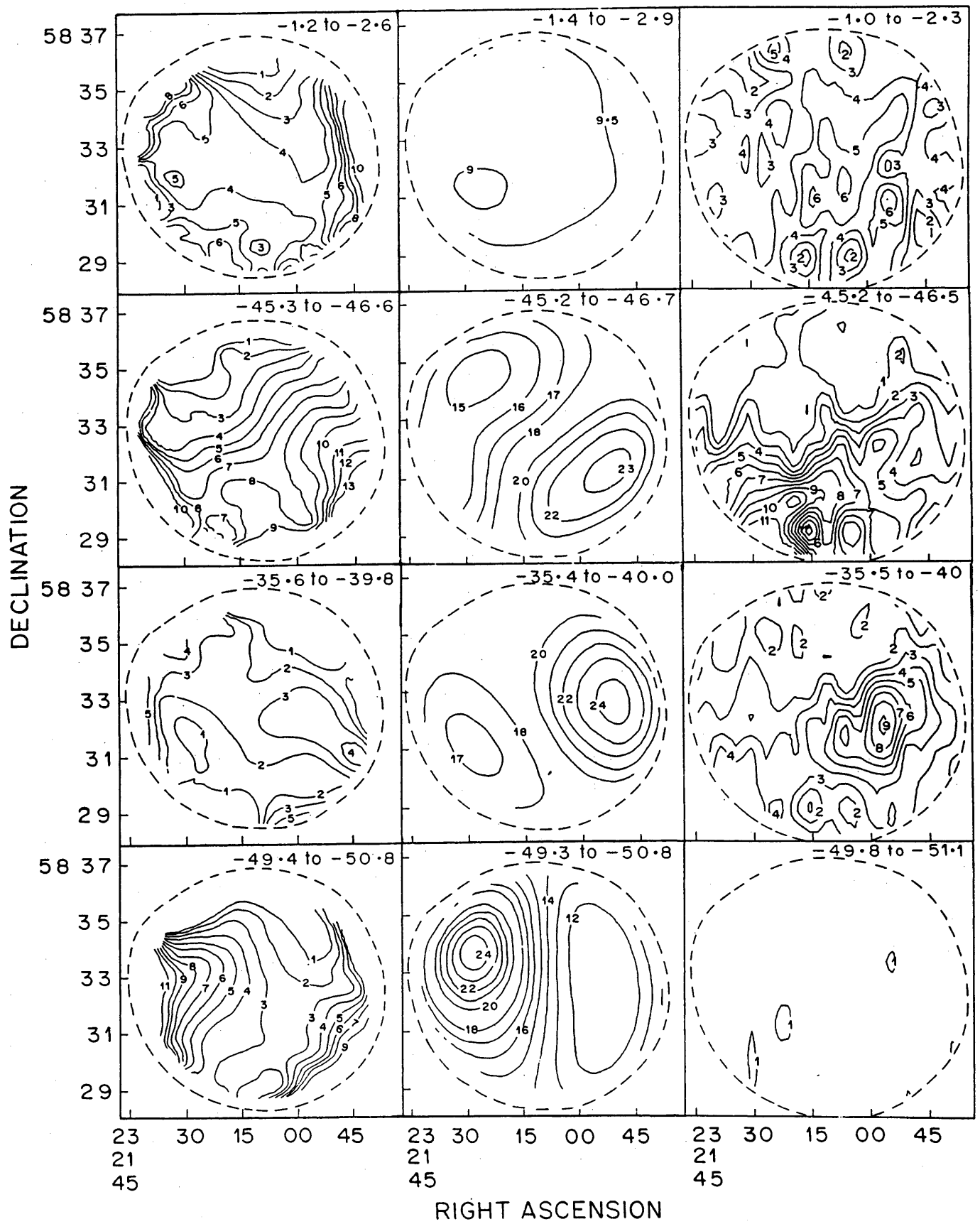

FIG. 11.—Variation in observed c270α (*left panels*), H I (*middle panels*), and ^{12}CO emission (*right panels*) across Cas A at different radial velocities. The gray-scale flux ranges from 0 to 5 K. The contour levels are 1, 2, 3, 4, 5, 6, 7, 8, 9, 10, 11, 13, and 15 in units of 0.3. The data are taken from Anantharamaiah et al. (1994).

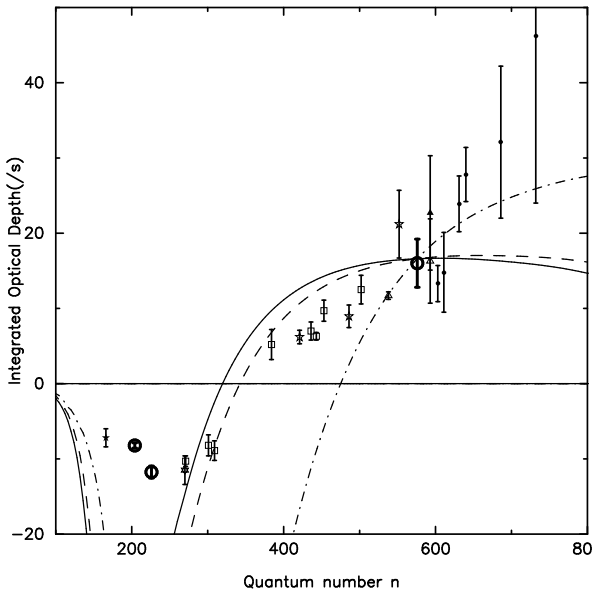

FIG. 12.—Cold gas models. Solid line is $T_e = 20$ K, $n_e = 0.65$ cm^{-3}, and $T_{R100} = 800$ K; dashed line is $T_e = 20$ K, $n_e = 0.46$ cm^{-3}, and $T_{R100} = 1600$ K, and dash-dotted line is $T_e = 20$ K, $n_e = 0.08$ cm^{-3}, and $T_{R100} = 3200$ K. The influence of dielectronic-like recombination process on the level populations has been included in these models. The data obtained by us at 34.5, 560, and 770 MHz are shown by bold circles.

our measurements of the integrated optical depths at 34.5, 560, and 770 MHz and the comparison, presented above, of the spatial distribution of the recombination line region with the molecular and H I regions in the direction of Cas A. To combine with our measurements, we use the corrected observational data at other frequencies tabulated by PAE94

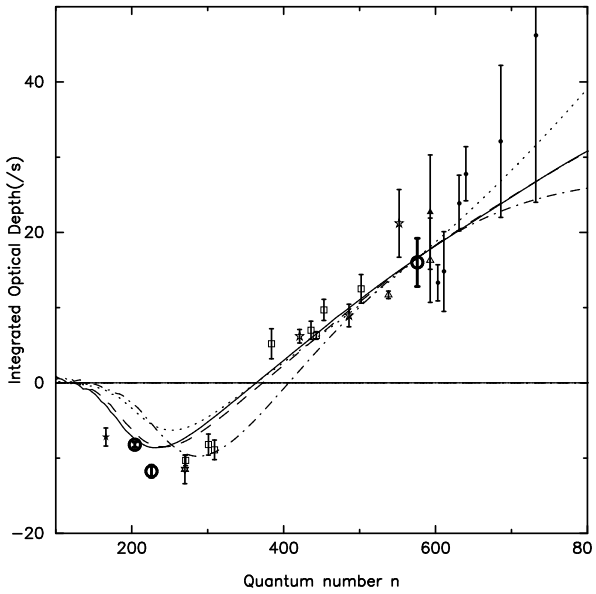

FIG. 13.—Warm gas models. Solid line is for $T_e = 75$ K, $n_e = 0.15$ cm^{-3}, and $T_{R100} = 800$ K; dashed line is for $T_e = 75$ K, $n_e = 0.11$ cm^{-3}, and $T_{R100} = 1600$ K; and dash-dotted line is for $T_e = 75$ K, $n_e = 0.02$ cm^{-3}, and $T_{R100} = 3200$ K. These models use the boundary condition $b_n \to 1$ as $n \to \infty$. The dotted curve is for $T_e = 35$ K, $n_e = 0.05$ cm^{-3}, and $T_{R100} = 800$ K, in which the level populations are calculated using the boundary condition $b_n \to 0$ as $n \to n_{\text{critical}}$. All these models are constrained by the emission measure calculated from our observed point at 34.5 MHz. The influence of dielectronic-like recombination process on the level populations has been included in these models.

and Sorochenko & Smirnov (1990). Since the two Perseus arm components at -39 and -47 km s^{-1} are blended into a single feature because of line broadening at lower frequencies, following PAE89 and PAE94, we consider only the total integrated optical depth of both the features. In Figure 12, we have shown all the available data from 14 MHz ($n = 768$) to 1400 MHz ($n = 165$) along with our measurements at 34.5 ($n = 578$), 560 ($n = 205$), and 770 MHz ($n = 205$). The symbols have the same meaning as for Figure 7.

To compare the data in Figure 12 with the predictions of a given model, specified by a combination of T_e and n_e, the expected integrated optical depth at different frequencies ν can be obtained from the following equation:

$$\int \tau_\nu d\nu = 2.046 \times 10^6 T_e^{-5/2} \exp\left[1.58 \times 10^5/(n^2 T_e)\right] \times \mathrm{EM} b_n \beta_n \ \mathrm{s}^{-1}, \quad (3)$$

(PAE94), where EM is the emission measure defined as $n_e n_{C^+} l$, l is the path length through the cloud, and b_n and β_n are the coefficients related to the departure of the level populations from LTE values. Modeling proceeds by first selecting a combination of T_e, n_e, and an appropriate background radiation temperature T_{R100}, which is consistent with the observed line width at 34.5 MHz as shown, for example, in Table 3. The departure coefficient b_n and its derivative β_n are computed for the selected combination of T_e, n_e, and T_{R100} using the computer code first developed by Salem & Brocklehurst (1979). This code was modified later by Walmsley & Watson (1982) to include the effects of a dielectronic-like recombination process in carbon suggested by Watson et al. (1980). The code was further modified by PAE94 to include the choice of an alternate boundary condition suggested by Gulyaev & Nefedov (1989) and to calculate the departure coefficients up to large quantum numbers ($n \sim 10{,}000$). The unknown emission measure, EM, in equation (3) is obtained by using our measured value of $\int \tau_\nu d\nu$ at 34.5 MHz.

Another physical quantity, the depletion factor of carbon, δ_c, enters the calculation indirectly. In considering the effect of the dielectronic-like process in carbon, the departure coefficients b_n and β_n depend on the relative population of the fine structure states $^2P_{1/2}$ and $^2P_{3/2}$ in carbon, which are involved in the process (Watson et al. 1980; Walmsley & Watson 1982; Ponomarev & Sorochenko 1992; PAE94). In turn, the relative population of $^2P_{1/2}$ and $^2P_{3/2}$ states depend on the density of electrons (n_e) and the density of neutral atoms (n_{H}). If we assume that all the electrons in the cloud are from ionization of carbon, then the neutral density is given by $n_{\mathrm{H}} = n_e/\delta_C(n_C/n_{\mathrm{H}})$, where $(n_C/n_{\mathrm{H}}) = 3 \times 10^{-4}$ is the cosmic abundance of carbon.

Using the modeling procedure outlined above, we now examine the two types of models (i.e., the cold gas model and the warm gas model) for the carbon line regions toward Cas A. The effect of the dielectronic-like process is included in both the models.

3.3.1. *Cold Gas Models*

In this model, we consider $T_e = 20$ K, which is the typical temperature in molecular clouds. The electron density n_e and the radiation temperature T_{R100} are chosen to be consistent with the observed line width at 34.5 MHz, as shown in Table 3. The three combinations of n_e and T_{R100} used in

TABLE 4

PARAMETERS OF VARIOUS MODELS IN FIGURES 12 AND 13

T_e (K)	n_e (cm^{-3})	T_{R100} (K)	EM (cm^{-6} pc)	S (pc)	δ_C	$n_H T_e$ (cm^{-3} K)	T_{Eq} (K)
	0.65	800	0.016	0.04	0.5	86667	21
20.....	0.46	1600	0.016	0.08	0.5	61333	21
	0.08	3200	0.019	3.44	0.5	10667	28
	0.15	800	0.018	0.76	0.5	75000	26
75.....	0.11	1600	0.016	1.32	0.5	55000	32
	0.02	3200	0.012	27.5	0.5	10000	56
75.....	0.101	1600	0.015	1.5	0.5	10500	29
35.....	0.05	800	0.004	1.6	0.6	9722	34

NOTE.—The model temperature and electron density shown in the last two rows of the table correspond to the best-fitting model parameters given by PAE94. The boundary condition $b_n \to 1$ as $n \to \infty$ is used for the model with $T_e = 75$ K, and the $b_n \to 0$ as $n \to n_{critical}$ condition is used for the model with $T_e = 35$ K; T_{Eq} is the equilibrium temperature.

these models are 0.65 cm^{-3} and 800 K, 0.46 cm^{-3} and 1600 K, and 0.08 cm^{-3} and 3200 K. In Figure 12, we have plotted the predicted variation of the integrated optical depth as a function of quantum number for these three models along with the observed data. The model parameters are given in Table 4. As seen in Table 4, for electron densities of 0.65 cm^{-3} and 0.46 cm^{-3}, the path length through the gas is 0.04 and 0.08 pc, respectively. However, none of the cold gas models provide a good fit to the observed data, as shown in Figure 12. All the three models predict very large optical depths near $n \sim 200$, which is not observed. While two of the models correctly predict the frequency of turnover from absorption to emission, neither of these models account for the observed line strengths at higher quantum numbers. In view of these difficulties, we do not favor the cold gas models in which the carbon line-forming region toward Cas A is assumed to be associated with molecular clouds in that direction.

3.3.2. *Warm Gas Models*

In the warm gas model, we consider $T_e = 75$ K, which is typical of the temperatures prevailing in neutral H I clouds. The electron density and the radiation temperature are again chosen to be consistent with the observed line width at 34.5 MHz. The three combinations of n_e and T_{R100} considered are 0.15 cm^{-3} and 800 K, 0.11 cm^{-3} and 1600 K, and 0.02 cm^{-3} and 3200 K. In Figure 13, the three models are superposed on the observed data, and the model parameters are given in Table 4. It is clear from Figure 13 that the warm gas models are able to provide much better fit to the data than the cold gas models. The general trend of the data is well accounted for by all the three models. The curves drawn in Figure 13 were all obtained by normalizing the emission measure using the data point at 34.5 MHz.

A visual inspection of Figure 13 shows that the higher electron density model (*solid line*, $n_e = 0.15$ cm^{-3}) gives a slightly better fit to the data than the lower density model (*dash-dotted line*, $n_e = 0.02$ cm^{-3}). The difference in these models is the radiation temperature. Although the higher density model provides a better fit to the data, the implied thermal pressure in the cloud is at least an order of magnitude higher than the thermal pressure in H I. As seen in Table 3, the thermal pressure (p/k) in this model is $\sim 3.7 \times 10^4$ cm^{-3} K, assuming that the depletion factor for carbon $\delta_C = 1$ (i.e., all the carbon is in gaseous phase). The actual thermal pressure is likely to be a factor of 2 higher, because carbon is known to be depleted onto grains and it is possible that $\delta_C \sim 0.5$ (see Table 4). This pressure is even higher than the total hydrostatic pressure of $\sim 24{,}000$ cm^{-3} K (Boulares & Cox 1990).

On the other hand, the thermal pressure in the lower density ($n_e = 0.02$ cm^{-3}) model in Figure 13 (*dash-dotted line*) is ~ 5000 cm^{-3} K (assuming $\delta_C = 1$), which is close to the range of thermal pressures observed in the ISM. Even if carbon is depleted onto grains with $\delta_C = 0.5$, the derived pressure in this model is within a factor of 2 of the interstellar value. Most of the gas in the Galaxy has a thermal pressure between 3000–5000 cm^{-3} K (McKee & Ostriker 1977; Kulkarni & Heiles 1980; Jenkins, Jura, & Loewenstein 1983). However, the pressure we obtain is less than the total hydrostatic pressure, and it is possible that in this case the total pressure is dominated by kinetic motion. As seen in Table 4, the path length through the gas in this low-density model is 27.5 pc, which is comparable to the lateral extent of the gas of >5 pc, and therefore a cloudlike geometry is permissible. In view of these desirable features, we favor this low-density model for the carbon line region in the direction of Cas A. The parameters of this model are as follows: $T_e = 75$ K, $n_e = 0.02$ cm^{-3}, $T_{R100} = 3200$ K, and EM = 0.011 pc cm^{-6}. This model fits the observed variation of line width and line intensity with frequency, predicts a turnover from emission to absorption at about the observed frequency, has an acceptable geometry for the line-forming region, and implies a thermal pressure in the cloud that is comparable to the pressure in the ISM. On the basis of these physical parameters (especially the temperature and density), we can identify these regions to be coexistent with the neutral H I clouds observed toward Cas A. This identification is consistent with the result of the previous section, in which the spatial distribution of the carbon line region over the face of Cas A was shown to have a good correspondence with the distribution of optical depth of the 21 cm H I line in this direction.

4. DISCUSSION OF MODELS

In searching for a model that could explain the various observations of low-frequency carbon recombination lines toward Cas A, we arrived above at a model in which the line-forming region has $T_e = 75$ K, $n_e = 0.02$ cm^{-3}, EM = 0.011 pc cm^{-6}, and up to 50% of carbon may be

depleted onto grains. This line-forming region is most likely associated with the neutral H I component in this direction. The thermal pressure in this model is less than the total hydrostatic pressure in the midplane.

It is actually remarkable that a simple model like this, where the density and temperature are assumed to be uniform, is able to explain most of the observations spanning about two decades in frequency. At the very least, this agreement between the model and the observations tell us that we are on the right track. Further refinements in both model and observations are of course always possible. Our model does not, in fact, give a perfect fit to the observed variation of optical depth with frequency (see Fig. 13), and this could be attributed to the simplicity of the model.

A similar model with slightly different parameters has been discussed by PAE94. They point out that one of the problems with the model is that the implied thermal pressure is too high compared to the pressure in the ISM. This problem is less severe in the model that we derive above: the thermal pressure is within a factor of 2 of the ISM value and much less than the total hydrostatic pressure in the midplane. But more importantly, and as pointed out earlier, it is not clear whether it is really necessary to require that these clouds be in complete thermal pressure equilibrium with the ISM. Recent high angular resolution observations of H I clouds using VLBI and other techniques (Diamond et al. 1989; Frail et al. 1994) have shown that the H I gas in the Galaxy has clumpiness on the scale of few tens of AU and that the thermal pressure in such clumps is very much higher than the interstellar pressure. Also high–angular resolution H I observations toward Cas A (Bieging et al. 1991) show structures on a variety of scales, again implying that the thermal pressures in these regions may be high. While these are outstanding problems in understanding interstellar H I that need to be pursued, they tell us that thermal pressure equilibrium is not a strict criterion to be applied for modeling the low-frequency recombination lines of carbon. In fact, if we relax this criterion, we can get a much better fit to the data in Figure 13 while still being consistent with the observed variation of line width with frequency (Fig. 13, *solid curve*).

PAE94 also point out a second problem with this type of model, which concerns the thermal balance in the line-forming region. PAE94 argue that if the carbon line-forming regions are associated with H I clouds, then it is possible to perform calculations to find the equilibrium temperature of the cloud by combining the physical parameters derived from the recombination line data with the results of H I observations at $\lambda 21$ cm. These calculations involve balancing the total heating by cosmic rays, photoelectric emission from grains, and polycyclic aromatic hydrocarbons with the cooling by collisional ionization, recombination, collisions with grains, and radiative transitions. Such a calculation was performed by PAE94 using the thermal models of Draine (1978), Shull & Woods (1985), and Verstraete et al. (1990). PAE94 show that the derived equilibrium temperature is at least a factor of 2 lower than the temperature that fits the recombination line data. In the last column of Table 4, equilibrium temperatures—which are calculated as described above with fractional ionization of hydrogen $X = 1 \times 10^{-4}$, ionization rate $\zeta_{\rm H} = 5 \times 10^{-17}$ s^{-1}, and polycyclic aromatic hydrocarbon (PAH) abundance $A_{\rm PAH} = 5 \times 10^{-7}$—have been listed. The models with temperatures near 75 K are clearly out of thermal balance, the equilibrium temperatures being much less. However, the necessary heating and cooling mechanisms appear to explain the temperature of 20 K which is used for the cold gas models. It appears that the actual situation is likely to be somewhere in the middle of these two models, corresponding to the boundary between neutral and molecular gas, described by photodissociation models (e.g., van Dishoeck & Black 1987; Tielens & Hollenbach 1985). The opacity of the 21 cm H I line goes as T^{-1}, while that of carbon recombination lines (neglecting non-LTE factors and assuming that all the electrons come from carbon atoms) goes as $T_e^{-5/2}$. So both favor cold regions. The similarity in the dependence on temperature means that in a medium with temperature inhomogeneities, 21 cm absorption lines and carbon recombination lines are likely to trace the same gas. In photodissociation models, the carbon is converted to neutral carbon and to CO, a short distance inside the transition from neutral to molecular hydrogen. Thus the neutral hydrogen and ionized carbon are expected to be nearly, but not entirely, cospatial and adjacent to regions of CO emission. The coldest, densest region containing ionized carbon is likely to be right at the edge of the molecular cloud.

PAE94 have provided evidence in favor of this picture by supporting the warm gas model, but at a fairly low temperature. In these models, the departure coefficients b_n and β_n are calculated by taking into account nonideal plasma effects on high–quantum number states, such as disruption of the levels by collisions with neutral atoms and electrons (Hummer & Mihalas 1988; Gulyaev & Nefedov 1989). These effects imply that at some large values of the quantum number n, the levels must be empty. This effect was quantified by PAE94 in terms of an "occupation probability," w_n, which is calculated from the physics of the particle interactions. The absence of bound states at high–quantum number levels is taken into account by changing the boundary condition for calculating the departure coefficients to $b_n \rightarrow 0$ as $n \rightarrow n_{\rm critical}$. This new class of models led PAE94 to a different set of parameters for the carbon line-forming regions toward Cas A. The model selected by them is displayed in Figure 13 as a dotted curve. The parameters of this model are $T_e = 35$ K, $n_e = 0.05$ cm^{-3}, $\delta_C = 0.6$, and $T_{R100} = 800$ K.

The desirable features of the new type of model by PAE94 are that (1) it fits the observed variation of optical depth of the carbon line with frequency reasonably well, (2) it is consistent with $\lambda 21$ cm H I absorption measurements in this direction, (3) it provides for thermal pressure equilibrium with the ISM, and finally (4) it passes the thermal balance check based on the heating and cooling rates in atomic clouds. However, this model does not explain one of the important observed parameters, namely, the variation of line width with frequency. The fitted parameters of this model (T_e, n_e, and T_{R100}) produce much less line broadening than observed at low frequencies. The variation of line width predicted by their model is shown as a triple-dot–dashed line in Figure 7. PAE94 left the resolution of this problem to future investigations.

We did not find any solution to this problem, although we tried a few variations in the computation of the departure coefficients using the modified boundary condition of PAE94. It is clear that nonideal plasma effects on the population of high–quantum number states are important for understanding low-frequency recombination lines, and it is

necessary to pursue such studies. At this stage, however, given the uncertainties in the calculation of thermal balance (many parameters are involved) and the mounting evidence for high thermal pressures in H I regions, we regard it as more important for the models to account for the observations than to completely satisfy the requirements of thermal and pressure balance. The model that we derived in the previous section does account for all the observations reasonably well, and the parameters of the model suggest that the regions could be in rough pressure equilibrium with the ISM. The model also suggests association with neutral H I clouds; this is well supported by the observations described in § 2.3, which shows a good correspondence between the spatial distribution of the optical depths of the H I 21 cm line and the C270α recombination line over the face of Cas A. Although the model does not provide thermal equilibrium, it is possible that a more refined treatment of the thermal balance calculation may indeed also satisfy this requirement.

5. SUMMARY

In this paper, we have presented the observation and interpretation of low-frequency carbon recombination lines toward Cas A and tried to derive a model of the line-forming region that could account for all the observations.

The high signal-to-noise absorption spectrum at 34.5 MHz obtained with the Gauribidanur array clearly showed a Voigt profile that is expected for pressure and/or radiation broadening and provided a reliable estimate of the integrated optical depth at this frequency. On considerations of radiation broadening, a lower limit of 115 pc was derived for the distance between Cas A and the absorbing clouds. The emission spectrum obtained at 770 MHz using the NRAO 140 foot telescope at Greenbank gave an estimate of the Doppler broadening of the line. The measured width of the -47 km s^{-1} feature at 560 MHz placed an upper limit of 3800 K on T_e, and the width of the -39 km s^{-1} feature in the 770 MHz spectrum places an upper limit of 7600 K. The measured Lorentzian width of the line at 34.5 MHz provided constraints on the combination of electron temperature, electron density, and radiation temperature in the line-forming region. The parameters suggested that the line-forming region could be associated with either molecular (H_2) or atomic (H I) gas in the direction of Cas A.

We then compared the spatial distribution of the C270α line over the face of Cas A, obtained using the VLA, with the distribution of ^{12}CO emission and also with the distribution of H I optical depth in that direction at an angular resolution of 1′. The comparison indicated that the carbon line-forming region in the direction of Cas A is more likely associated with the atomic H I gas rather than the molecular (H_2) gas.

We combined our data with other available observations toward Cas A in the frequency range 14–1400 MHz and explored two types of models, the cold gas model and the warm gas model, to explain the observed variation of line width and line strength over the entire frequency range. In both the models, we considered only the combinations of electron temperature, electron density, and radiation temperature that were constrained by the observed width of the line at 34.5 MHz. We found that the cold gas model (T_e = 20 K), which implicitly assumes the association of the carbon line region with molecular clouds, does not fit the observations. On the other hand, the warm gas model (T_e = 75 K), provides good fit to the data and thus supports the scenario in which the carbon lines are formed in neutral H I regions in the direction of Cas A. The fitted parameters of the model are T_e = 75 K, n_e = 0.02 cm^{-3}, T_{R100} = 3200 K, and EM = 0.011 cm^{-6} pc. These parameters imply that the line-forming regions are in rough pressure equilibrium in the ISM.

We end with a discussion of an alternative model presented by PAE94, in which the departure coefficients b_n and β_n were computed after taking into account nonideal plasma effects on the population of high–quantum number states. Although this model has a number of desirable features, it does not account for the observed variation of line width with frequency.

The National Radio Astronomy Observatory is a facility of the National Science Foundation operated under cooperative agreement by Associated Universities, Inc. We thank A. Santosh Kumar and T. S. Ravishankar for the construction and testing of the multiline spectrometer used at 34.5 MHz.

REFERENCES

Anantharamaiah, K. R., Erickson, W. C., Payne, H. E., & Kantharia, N. G. 1994, ApJ, 430, 682
Baars, J. W. M., Genzel, R., Pauliny-Toth, I. I. K., & Witzel, A. 1977, A&A, 61, 99
Bieging, J. H., Goss, W. M., & Wilcots, E. M. 1991, ApJS, 75, 999
Blake, D. H., Crutcher, R. M., & Watson, W. D. 1980, Nature, 287, 707
Boulares, A., & Cox, D. P. 1990, ApJ, 365, 544
Deshpande, A. A., Shevgaonkar, R. K., & Shastry, Ch. V. 1989, J. Inst. Electron. Telecommunications Eng., 35, 342
Diamond, P. J., Goss, W. M., Romney, J. D., Booth, R. S., Kalberla, P. M. W., & Mebold, U. 1989, ApJ, 347, 302
Draine, B. T. 1978, ApJS, 36, 595
Ershov, A. A., Ilyasov, Yu. P., Lekht, E. E., Smirnov, G. T., Solodkov, V. T., & Sorochenko, R. L. 1984, Soviet Astron. Lett., 10, 348
Ershov, A. A., Lekht, E. E., Smirnov, G. T., & Sorochenko, R. L. 1987, Soviet Astron. Lett., 13, 8
Frail, D. A., Weisberg, J. M., Cordes, J. M., & Mathers, C. 1994, ApJ, 436, 144
Gulyaev, S. A., & Nefedov, S. A. 1989, Astron. Nachr., 310, 403
Haslam, C. G. T, Stoffel, H., Salter, C. J., & Wilson, W. E. 1982, A&AS, 47, 1
Hummer, D. G., & Mihalas, D. 1988, ApJ, 331, 794
Jenkins, E. B., Jura, M., & Loewenstein, M. 1983, ApJ, 270, 88
Konovalenko, A. A. 1984, Soviet Astron. Lett., 10, 353
———. 1990, in Radio Recombination Lines: 25 Years of Investigation, ed. M. A. Gordon & R. L. Sorochenko (Dordrecht: Kluwer), 175
Konovalenko, A. A., & Sodin, L. G. 1980, Nature, 283, 360
———. 1981, Nature, 294, 135
Kulkarni, S., & Heiles, C. 1988, in Galactic and Extragalactic Radio Astronomy, ed. G. H. Verschuur & K. I. Kellerman (Berlin: Springer), 95
Lekht, E. E., Smirnov, G. T., & Sorochenko, R. L., 1989, Soviet Astron. Lett., 15, 171
McKee, C., & Ostriker, J. 1977, ApJ, 196, 565
Payne, H. E., Anantharamaiah, K. R., & Erickson, W. C. 1989, ApJ, 341, 890 (PAE89)
———. 1994, ApJ, 430, 690 (PAE94)
Ponomarev, V. O., & Sorochenko, R. L. 1992, Soviet Astron. Lett., 18, 215
Ravindra, D. K. 1983, Ph.D. thesis, Indian Institute of Science, Bangalore
Salem, M., & Brocklehurst, M. 1979, ApJS, 39, 633
Schwarz, U. J., Goss, W. M., & Kalberla, P. M. W. 1997, A&AS, 123, 43
Shaver, P. A. 1975, Pramana, 5, 1
Shull, M. J., & Woods, D. T. 1985, ApJ, 288, 50
Sorochenko, R. L., & Smirnov, G. T. 1990, in Radio Recombination Lines: 25 Years of Investigation, ed. M. A. Gordon & R. L. Sorochenko (Dordrecht: Kluwer), 189
Sorochenko, R. L., & Walmsley, C. M. 1991, Astron. Astrophys. Trans, 1, 31
Tielens, A. G. G. M., & Hollenbach, D. J. 1985, ApJ, 291, 722
Udayshankar, N. 1986, Ph.D. thesis, Bangalore Univ.
van Dishoeck, E. F., & Black, J. H. 1987, in Physical Processes in Interstellar Clouds, ed. G. E. Morfill & M. Scholer (NATO ASI Ser.; Dordrecht: Reidel), 241
Verstraete, L., Leger, A., d'Hendecourt, L., Dutoit, O., & Defourneau, D. 1990, A&A, 237, 436
Walmsley, C. M., & Watson, W. D. 1982, ApJ, 260, 317
Watson, W. D., Western, L. R., & Christensen, R. B. 1980, ApJ, 240, 956